Macromolecules

pubs.acs.org/Macromolecules Article

Quantification of Dispersion for Weakly and Strongly Correlated Nanofillers in Polymer Nanocomposites

Alex McGlasson,[⊥] Kabir Rishi,[⊥] Gregory Beaucage,* Michael Chauby, Vikram Kuppa, Jan Ilavsky, and Mindaugas Rackaitis

Cite This: *Macromolecules* 2020, 53, 2235−2248 Read Online

ACCESS | Metrics & More | Article Recommendations | Supporting Information

ABSTRACT: The dispersion of nanoparticles in viscous polymers is dictated by kinetics, interaction potentials between particles, and interfacial compatibility between the matrix and dispersed phases. It was previously proposed that an analogy can be made between thermally dispersed colloids and kinetically dispersed nanoparticles in viscous media when weak interactions exist between particles allowing for a mean-field description under the Ginzburg criterion such as for carbon black dispersed in polybutadiene elastomer. For these cases, the second virial coefficient can be used to quantify the quality of dispersion; additionally, the nanoscale network mesh size can be calculated, which is related to dynamic properties. However, this approach fails for nanoparticles with surface charges or other specific interactions that lead to correlations. Here, these correlated systems are investigated in the context of the mean-field systems in order to gain a comparative description of dispersion using the network mesh size and a derived virial coefficient. The physical origin of the structural parameters from the proposed model for these correlated systems is investigated.

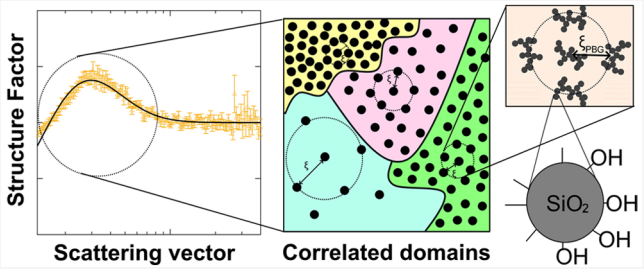

INTRODUCTION

In nanocomposites, reinforcing nanofillers can drastically alter the bulk properties of the matrix. For example, carbon black can turn a soft flexible elastomer, such as polybutadiene, into a stiff, tear-resistant material that can be used in tire compounds.[1] While the theoretical strength of composites such as nanotube and nanoplatelet-reinforced structures is enormous, this theoretical reinforcement is not found partially because of poor dispersion.[2−4] High surface area materials tend to minimize their surface area by clustering and agglomeration. This tendency can be opposed by mechanical dispersion, compatibilization of the nanofiller with the matrix phase, and repulsion between the dispersed nanoparticles. The structural impact of these approaches can be complex.[5−7]

Commercial reinforced polymers generally use nanostructured, aggregated fillers such as silica, carbon black, zirconia, titania, and other solution-grown or flame-synthesized oxides. Similar structures are seen with some additives such as organic pigments and flame retardants. These common industrial fillers have hierarchical structures, typically with three structural levels—level 1: primary particle; level 2: aggregates of primary particles; and level 3: agglomerates of aggregates. During nanoparticle synthesis, primary particles fuse together to form aggregates that cluster together to form agglomerated or micron-scale network structures. During mixing, agglomerates can break up into aggregate substructures; however, aggregates will not break apart into primary particles. The mixing process imparts sufficient energy to overcome van der Waal's forces holding together agglomerates on the micron scale, but it lacks sufficient energy to break apart the fused aggregates on the nanoscale.[8,9] If the system is sufficiently dilute, below ϕ^* of about 1 wt % nanofiller, the morphology and size of these hierarchical moieties can be ascertained from the dilute-reduced (concentration-normalized) scattered intensity $\left(\frac{I_0(q,\phi_0)}{\phi_0}\right)$ using the Unified Scattering Function,[10−12]

$$\frac{I_0(q,\phi_0)}{\phi_0} = \sum_{i=1}^{n}\left[G_i \exp\left(\frac{-q^2 R_{g,i}{}^2}{3}\right) + B_i (q_i^*)^{-P_i} \exp\left(\frac{-q^2 R_{g,i-1}{}^2}{3}\right)\right] \quad (1)$$

$$q_i^* = \frac{q}{[\mathrm{erf}(kqR_{g,i}/\sqrt{6})]^3} \quad (2)$$

where "i" is the structural level, G_i and B_i are the Guinier and Porod prefactors related to number density of scatters and the surface-to-volume ratio for structural level "i", respectively, $R_{g,i}$

Received: November 19, 2019
Revised: January 19, 2020
Published: March 13, 2020

https://dx.doi.org/10.1021/acs.macromol.9b02429
Macromolecules 2020, 53, 2235−2248

is the radius of gyration, P_i is the power law exponent, and q is the reciprocal space vector. R_g is a measure of the size of a specific nanofiller hierarchical structure while P is related to the morphology of that structural feature. The reciprocal space vector, q, is inversely related to the spatial dimension (r), so high values of q are related to small structural features and vice versa. "erf", in eq 2, is the error function and k is a constant equal to 1 for solid primary particles and is approximately equal to 1.06 for mass fractal aggregates. 1.06 is obtained from an integral of the correlation function for a mass fractal of dimension 2.[10] It could have slightly different values depending on the mass fractal dimension but is within 1% of this value for all mass fractal aggregates. After dispersion of agglomerates, nanoaggregates can reassemble into local networks depending on the kinetic energy imparted to the system during mixing and the repulsion or attraction of the nanoparticles. At larger sizes, this reassembly is hindered by mechanical mixing because longer lever arms can break apart the nascent clusters. Under semidilute concentrations, these clusters can percolate into a micron-scale network in a dual-network hierarchy as described by Rishi et al.[5]

Although the Unified Scattering Function can be used to model the structure of nanoaggregates (level 2) at concentrations below ϕ^* (dilute), the function lacks a description of the distribution of the nanoaggregates relative to one another above ϕ^* (semidilute). To describe this distribution, various correlation functions with different closure relationships are used. A combination of these correlation functions with their respective closure relationships have been applied to a wide variety of systems ranging from thermally dispersed colloids to kinetically dispersed polymer nanocomposites.[13−16] The Ornstein and Zernike function in eq 3 generalizes the interactions of particles in the liquid state such that the total correlation function,[17]

$$h(r) = c(r) + \rho \int c(|\vec{r} - \vec{r'}|)h(r')\, \mathrm{d}^3\vec{r'} \tag{3}$$

is the sum of the direct binary correlations, $c(r)$, plus the effect of higher order interactions, expressed as a convolution of $h(r)$ and $c(r)$ over all distances r. Here, ρ indicates the number density of particles/nanoaggregates.

While the Ornstein−Zernike expression provides a description of the total interactions within a system, obtaining a solution to the expression is quite difficult. To solve the expression, various closure relationships must be employed because the function is recursive as written. These closure relationships make assumptions about the system and provide a solution restricted to those conditions. In general, these closure relationships either assume mean-field interactions or account for specific interactions between particles. Three commonly used closure relationships for the Ornstein−Zernike expression in eq 3 are the random-phase approximation (RPA),[18] the Percus−Yevick approximation,[19] and the Born−Green approximation.[20]

Weak Correlations: A Mean Field Model via the RPA. Nanocomposites that contain nanofillers that do not display specific interactions follow a mean-field model characterized by the absence of a correlation peak in scattering. Wang et al. classified polymer−filler interactions based on their surface energies as determined by inverse gas chromatography.[21,22] Surface energy is sensitive to the chemical constitution and the microstructure of the nanofillers. It was split into a dispersive and a specific polar component with a larger dispersive component indicating favorable polymer−filler interactions.[23] For carbon black in an elastomer, a smaller specific polar component of surface energy indicates weaker filler−filler interactions and the behavior of these nanoaggregates above ϕ^* can be modeled by a mean-field approach. The reduced scattered intensity $\left(\frac{I(q,\phi)}{\phi}\right)$ can be modeled using the RPA,[5,13−15]

$$\left(\frac{I(q,\phi)}{\phi}\right)^{-1} = \left(\frac{I_0(q,\phi_0)}{\phi_0}\right)^{-1} + \phi\upsilon \tag{4}$$

where ϕ is the volume fraction of the nanofiller in the nanocomposite above ϕ^*, whereas ϕ_0 is the volume fraction of a dilute sample below ϕ^*. The extent of structural screening, $\phi\upsilon$, is a measure of the loss of normalized scattering due to overlap of structural features as illustrated in Figure 1b. The screening parameter, υ, is independent of the nanofiller volume fraction with larger values indicating better dispersion. In terms of scattered intensity, the structure factor is defined as,

$$S(q) = \frac{\frac{I(q,\phi)}{\phi}}{\frac{I_0(q,\phi_0)}{\phi_0}} \tag{5}$$

such that a mean-field system as modeled by the RPA yields,

$$S_{\mathrm{RPA}}(q) = \frac{1}{1 + \phi\upsilon(I_0(q,\phi_0)/\phi_0)} \tag{6}$$

The above expression provides a simple method to determine the screening parameter, υ, for systems where interactions can be modeled via a mean field. The value of υ reflects the interactions between particles and is directly related to the value of the pseudo-second virial coefficient, A_2, through,[14,15]

$$A_2 = \frac{\upsilon\langle\Delta\rho\rangle^2}{2N_A(\rho_f)^2} \tag{7}$$

where $\langle\Delta\rho^2\rangle$ is the squared difference in scattering length density between the nanofiller and the nanocomposite matrix or the scattering contrast, N_A is Avogadro's number, and ρ_f is the bulk density of the filler. Under semidilute conditions, overlapping nanoaggregates form a nanoscale network characterized by the mesh size, ξ_{RPA}, that can be determined through the intersection of $1/(\phi\upsilon)$ with the normalized dilute scattering curve at q_{RPA} such that $\xi_{\mathrm{RPA}} = 2\pi/q_{\mathrm{RPA}}$, as shown in Figure 1b. The mesh size, ξ_{RPA}, is the average spacing between nanoaggregates.

For colloidal particles suspended by thermal energy, such as aqueous dispersions of organic pigments with nonionic surfactants,[13] close to a random distribution of particles is obtained that follows a mean-field description and can be quantified using the second virial coefficient, A_2. Some kinetically dispersed systems, such as carbon black in polybutadiene, approximate the mean-field behavior. During mixing, the agglomerates are broken apart but try to re-cluster in opposition to kinetic mixing. On the nanoscale, aggregates cluster in a nanonetwork at about 5 vol % and these nanonetwork clusters percolate into a micron-scale network at about 20 vol %. The nanoscale network is linked to the dynamic mechanical response at low strain while the micron-scale network of clusters is responsible for the Payne effect at

https://dx.doi.org/10.1021/acs.macromol.9b02429
Macromolecules 2020, 53, 2235−2248

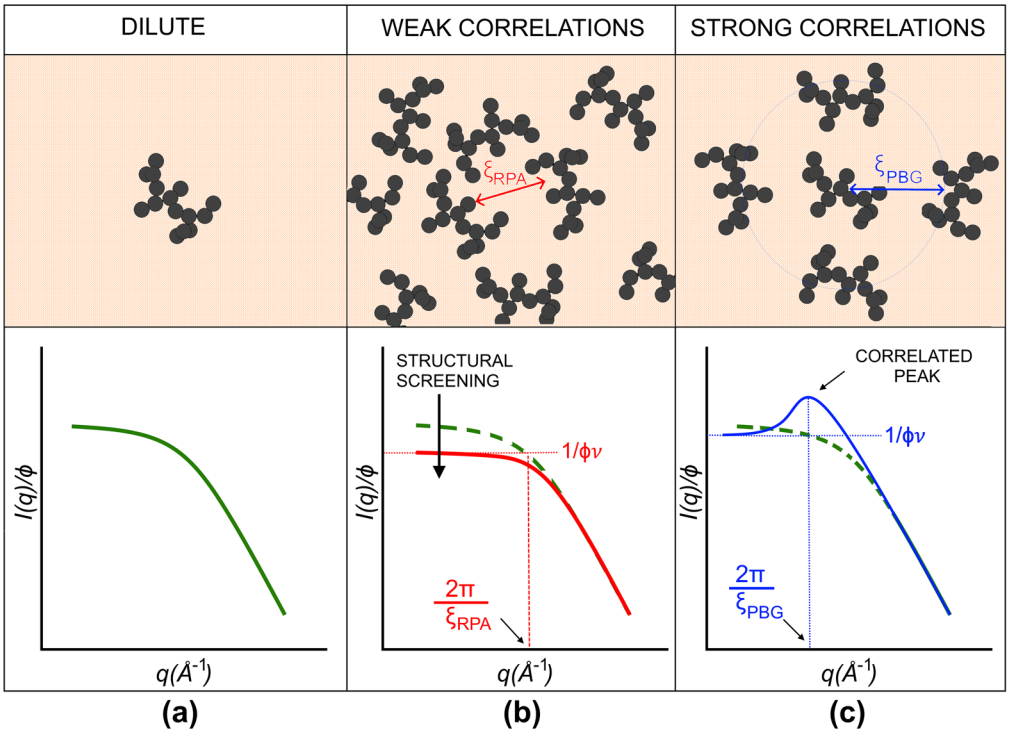

Figure 1. (a) Typical scattering profile for filled polymers under dilute conditions; (b) mean-field approach modeled via the RPA, eq 4, for nanoaggregates with no correlation of structure under semidilute conditions such that A_2 can be determined from the low-q reduced intensity; and (c) specific interactions resulting in a correlation peak in reduced scattered intensity under semidilute conditions modeled via a modified Born−Green approach wherein the reciprocal scattering vector $q_{PBG} = 2\pi/\xi_{PBG}$ is used in conjunction with the dilute curve to determine A_2.

large strain amplitude.[5−7] Small-angle X-ray scattering (SAXS) and the RPA have been used to obtain the pseudo-second virial coefficient, A_2, in these mean-field systems.[5,13−16] Positive values of A_2 indicate good dispersion, and negative values of A_2 indicate phase separation. A_2 has also been used to determine the potential function for coarse grain simulations.[14] The mesh size of the nanoscale network, ξ, can be obtained from the dilute scattering curve, the filler concentration, and the value of A_2 as described above.

Strong Correlations: A Specific Interaction Model via a Polydisperse Born−Green Approximation (PBG). For nanofillers with significant surface charge, the RPA is no longer appropriate since a peak is observed in scattering.[8,9,14,24−28] Although electrostatic effects leading to correlations in a low dielectric media such as in a polymer matrix are not obvious, several recent papers that deal with this subject theoretically result in the prediction of moderate electrostatic forces over about 4 μm between two weakly charged spheres.[29,30] In silica, the electrostatic charge varies because of the density of silanol functional groups on the surface, which is greater for precipitated silica than for colloidal silica and the least for fumed silica.[31] A larger surface charge leading to increased repulsive interactions between the nanoaggregates presents a correlation peak in the SAXS pattern, although these correlation peaks were absent when fumed silica was coated with carbon.[32] As opposed to carbon black, the precipitated silica in elastomers displays strong filler−filler interactions.[23] At concentrations above ϕ^*, specific interactions due to surface charge lead to correlated structures on the nanoscale as illustrated in Figure 1c. At intermediate q, a peak appears to be associated with the packing/correlation distance between aggregates. At higher concentrations, the peak moves to higher q (smaller size) and becomes sharper, reflecting more order and shorter correlation distances.

The Percus−Yevick approximation is a commonly used closure relationship for the Ornstein−Zernike expression and has been used to describe the dispersion of hard spheres within a matrix. This expression is utilized for monodisperse spherical colloidal silica. An analytic solution to the direct binary correlations, $c(r)$, in the Ornstein−Zernike expression in eq 3 was given by Wertheim[33] as

$$c(r) = -\alpha - \beta(r/\xi) - \delta(r/\xi)^3 \tag{8}$$

where $\alpha = \frac{(1+2\phi)^2}{(1-\phi)^4}$, $\beta = -6\phi\frac{(1+0.5\phi)^2}{(1-\phi)^4}$, $\delta = \frac{\alpha\phi}{2}$, and ξ is the mean distance between the spherical particles. The Fourier transform of the binary correlation function in eq 8 is,

$$\rho C_{PY}(q,\xi) = -24\phi\left\{\alpha\left(\frac{\sin(q\xi) - (q\xi)\cos(q\xi)}{(q\xi)^3}\right) - \beta\left(\frac{(q\xi)^2\cos(q\xi) - 2(q\xi)\sin(q\xi) - 2\cos(q\xi) + 2}{(q\xi)^4}\right) - \delta\left(\frac{(q\xi)^4\cos(q\xi) - 4(q\xi)^3\sin(q\xi) - 12(q\xi)^2\cos(q\xi) + 24(q\xi)\sin(q\xi) + 24\cos(q\xi) - 24}{(q\xi)^6}\right)\right\} \tag{9}$$

https://dx.doi.org/10.1021/acs.macromol.9b02429
Macromolecules 2020, 53, 2235−2248

Additionally, from the convolution theorem,[34] the Fourier transform of eq 3 given by $H(q) = C(q) + \rho H(q)C(q)$ is used to determine the interparticle structure factor as,

$$S_{PY}(q, \xi) = \frac{H(q)}{C(q)} = \frac{1}{1 - \rho C_{PY}(q, \xi)} \quad (10)$$

Combining eqs 9 and 10, the average interparticle spacing from the Percus−Yevick function, ξ_{PY}, can be determined from fits to the structure factor described in eq 10.

McEwan et al.[35] quantified the impact on particle interactions of polydimethylsiloxane (PDMS) brushes grafted onto colloidal silica nanoparticles in PDMS matrices of varying molecular weights. SAXS was used to ascertain the structure factor, $S(q)$, and a Fourier transform was used to compute the radial distribution function, $g(r)$. The particle interaction potential, $U(r)$, could then be obtained from $g(r)$ after employing the Percus−Yevick approach described above, although polydispersity in the interparticle distance complicated the approach.

Baeza et al.[8] considered a modification of the Percus−Yevick approximation to quantify the dispersion of precipitated silica in styrene−butadiene rubber (SBR) via SAXS. They simulated the correlated structures as aggregates that change under semidilute concentrations while considering polydispersity in primary particle and aggregate size to account for a distribution in correlation distances. The structure factor, $S(q)$, was determined by normalizing the measured scattered intensity by a simulated form factor (dilute scattering intensity vs q). This reduced structure factor was fit with an arbitrary power law function that allowed for quantification of $S(q = 0)$ analyzed by the modified Percus−Yevick closure at $q = 0$. Bouty et al.[9] performed similar studies to Baeza et al.[8] on colloidal silica in SBR. Rather than simulating the correlated aggregate structure and interactions within, the structure factor was fit to the analytical solution of the Percus−Yevick integral equation developed by Wertheim[33] described in eqs 9 and 10. The fits described the experimental structure factor over an extremely narrow range in q that could neither reproduce the correlation peak nor the low-q behavior. In a later study, Bouty et al.[24] used a similar model system to understand the effects of chain conformation on nanoparticle dispersion, wherein it was demonstrated that colloidal silica nanoparticles act as additional cross-linking sites that prevent chain relaxation within the nanocomposite. However, a Percus−Yevick fit was not attempted.

The Born−Green closure of the Ornstein−Zernike equation was first proposed to describe the distribution of hard spheres similar to the Percus−Yevick closure described above. However, the solution is significantly less cumbersome and yields comparable results to the Percus−Yevick approximation. Beaucage et al. proposed the use of the Born−Green closure for in situ silica PDMS nanocomposites.[25] The Born−Green closure is given by,[20]

$$S_{BG}(q, \xi) = \frac{1}{1 + p\theta(q, \xi)} \quad (11)$$

where the packing factor, p, is the ratio of the average "hard-core" volume of the filler to the total volume multiplied by 8, and ξ is the correlation distance. The packing factor reflects the adherence to organization in a spherical shell through the ratio of occupied to available volume. For spherical particles, p varies from 0, indicating no correlations, to 5.92, for closest packed structures. However, for mass fractal aggregates, p can have much higher values because the asymmetric nanoaggregates can align and possibly interpenetrate, resulting in a higher packing density than spheres. For example, p could be a very large number for highly asymmetric objects such as lamellae. The function $\theta(q,\xi)$ is the spherical amplitude function given by,[20]

$$\theta(q, \xi) = 3\left(\frac{\sin(q\xi) - q\xi\cos(q\xi)}{(q\xi)^3}\right) \quad (12)$$

which reflects the organization of nearest-neighbor aggregates in a rough sphere around an aggregate as shown in Figure 1c. Note that eq 12 is similar to the first term in eq 9. At $q = 0$, $\theta = 1$ and the structure factor in eq 11 is $S_{BG}(0,\xi) = 1/(1 + p)$. This means that the breadth of the correlation peak, as controlled by the packing factor, p, determines the $q \rightarrow 0$ intercept for the structure factor, so determination of the $q \rightarrow 0$ intercept relies on a description of the shape of the structure factor at the peak in cases where the low-q data cannot be observed because of agglomeration of aggregates.

Equations 11 and 12 were used to describe the correlations between in situ prepared silica nanoaggregates in filled PDMS produced via a sol−gel process in which silica was generated from the excess cross-linking agent, tetraethyl orthosilicate.[25] The system had significant mobility because the initial prepolymers were of relatively low molecular weight and viscosity. This allowed for a regular separation of aggregates and a close to uniform correlation distance as depicted in Figure 2a. On the contrary, in kinetic dispersions, milling of nanocomposites results in nonuniform accumulated strain as indicated by McEwan et al.[35] and Baeza et al.[8] Further, it is expected that the variation in accumulated strain will form domains of correlation with different correlation distances as depicted in Figure 2b. Evidence for domains of correlation can be found in the transmission electron micrographs of both precipitated and colloidal silica.[8,9]

In kinetically mixed systems with charged nanofillers, correlation results form a balance between the accumulated strain and the repulsive charge. Because the accumulated strain varies with position because of nonuniform mixing, domains of correlation with a distribution of correlation distances occur, as illustrated in Figure 2b. To account for domains with different correlation lengths, ξ, a log−normal distribution, $P(\xi)$,[11,36] of correlation distances is proposed,

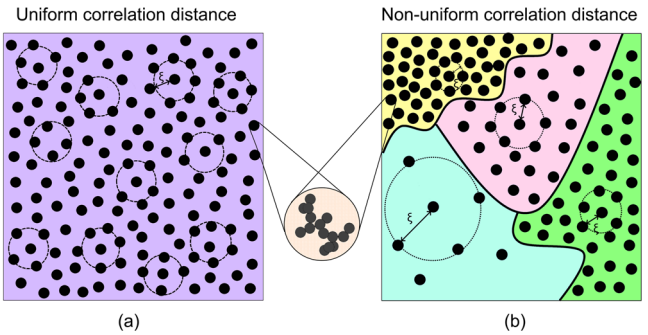

Figure 2. (a) Uniform correlation distance in low MW polymers with easy transport of growing silica aggregates[25] and (b) nonuniform correlation distances for nanofillers in a highly viscous milled elastomer due to differences in accumulated strain leading to domains of correlation.

https://dx.doi.org/10.1021/acs.macromol.9b02429
Macromolecules 2020, 53, 2235−2248

$$P(\xi) = \frac{1}{\sqrt{2\pi}\xi\sigma} \exp\left(\frac{-\{\ln(\xi/m)\}^2}{2\sigma^2}\right) \quad (13)$$

$$m = \langle\xi\rangle_{PBG} \exp(-\sigma^2/2) \quad (14)$$

The structure factor is then given by,

$$S_{PBG}(q, \xi) = \int_0^\infty P(\xi)\left[\frac{1}{1 + p\theta(q, \xi)}\right] d\xi \quad (15)$$

Equation 15 describes the domains of correlated particles with different ξ. Thus, the value of $\langle\xi\rangle_{PBG}$ obtained from the fits is an average distance between structural features across different domains of correlation. Equation 15 is obviously a gross simplification of a rather complex structure but seems to be a reasonable approximation for dispersed silica aggregates in elastomers.

For weakly correlated systems such as carbon black in polybutadiene, $\phi\upsilon$ is determined from the RPA equation, eq 6. The intersection of $1/(\phi\upsilon)$ with the dilute-reduced scattering curve, $\left(\frac{I_0(q,\phi_0)}{\phi_0}\right)$, occurs at q_{RPA}. Then, q_{RPA} is used to calculate the nanonetwork mesh size, $\xi_{RPA} = 2\pi/q_{RPA}$. However, for strongly correlated, kinetically dispersed systems, the correlation distance averaged over all domains, $\langle\xi\rangle_{PBG}$, is obtained from eqs 13−15. This can be used to determine an average reciprocal spacing vector, $q_{PBG} = 2\pi/\langle\xi\rangle_{PBG}$, over the size distribution of domains. q_{PBG} coupled with the Unified fit parameters from the dilute scattering curve can be used to determine the second virial coefficient, A_2, for these systems. Following Rishi et al.,[5] υ can be calculated from,

$$(1/\phi\upsilon) = \left\{G_2 \exp\left(\frac{-q_{PBG}{}^2 R_{g,2}{}^2}{3}\right) + \exp\left(\frac{-q_{PBG}{}^2 R_{g,1}{}^2}{3}\right) B_2 (q^*_{PBG,2})^{-P_2}\right\} + \left\{G_1 \exp\left(\frac{-q_{PBG}{}^2 R_{g,1}{}^2}{3}\right) + B_1 (q^*_{PBG,1})^{-P_1}\right\} \quad (16)$$

As the filler volume fraction, ϕ, in the nanocomposite is known, υ can be obtained. Additionally, υ is related to A_2 through eq 7. υ can also be determined from $S(q = 0)$ using the fitting parameters acquired from eq 15, but in immiscible aggregate nanocomposites, the $q = 0$ extrapolation is obscured by large-scale agglomerates.[26]

The approaches presented in this article allow for a direct comparison of the nanoscale quality of dispersion, through A_2, for both weakly and strongly correlated fillers in nanocomposites. For kinetically dispersed nanocomposites, a measure of the correlation length via currently available techniques is unfeasible, and a promising methodology has been proposed. In this paper, these techniques will be used to compare the dispersion of systems that display correlated and mean-field behavior using A_2 and the mesh size, ξ. A measure of A_2, thus obtained, can further be used as an input for coarse-grained dissipative particle dynamic simulations.[14] In the past, systems with specific interactions, that is, those that display a correlation peak in scattering,[14] were not evaluated because the tools described in this paper were not available. Here, the feasibility of the proposed techniques is tested on these systems from the literature. While it is recognized that dispersion on the nanoscale represents a significant challenge in application, a quantitative measure of dispersion on the nanoscale is needed in order to understand and rank the impact of surface treatments, processing, surface charge, and matrix modification. Further, the impact of nanoscale dispersion on the emergence of multihierarchical structures such as micron-scale networks of nanoscale aggregates could be understood and manipulated if the underlying nanoscale dispersion could be quantified. This serves as the motivation for this study, especially for the comparison of nanodispersion for systems of differing interaction type, that is, subject to mean-field or specific interactions.

EXPERIMENTAL SECTION

Filled nanocomposites were prepared in a 50 g Brabender mixer with a Banbury style mixing geometry. The precipitated silica and carbon black samples were sheared at a constant rotor speed of 60 rpm for 20 and 24 min, respectively. The temperature within the mixing chamber, controlled using an air-cooling stream, varied between 121 °C (250 °F) and 130 °C (266 °F) during the mixing process. Samples were prepared with filler concentrations of 1 wt % ($\phi \approx 0.005$) and 16 wt % ($\phi \approx 0.08$), whereas for carbon black nanocomposites, an additional concentration of 5 wt % ($\phi \approx 0.03$) was prepared. The matrix polymers were from various grades of commercial SBR as detailed in Table 1. The fillers used in this study were commercially available as Hi-Sil 190G, supplied by PPG Industries, and Vulcan 8 carbon black, supplied by Cabot Corporation. The nanocomposites also contained an antioxidant, (*N*-(1,3-dimethylbutyl)-*N*′-phenyl-1,4-phenylenediamine), which was provided by TCI America. The raw material properties are listed in Table 1. The mixing sequence entailed milling the matrix polymer until the temperature equilibrated to a constant value, followed by addition of the antioxidant and mixing for 30 s. Upon completion of this 30 s period, the filler was charged to the mixer and the system was sheared for 20 or 24 min for precipitated silica and carbon black samples, respectively.

Table 1. Raw Material Properties and Designation for Samples

material	material specification	designation	density (g/cc)	Mooney viscosity
polymer matrix	SBR	4526HM	0.94	62
		4526	0.94	50
reinforcing nanofillers	precipitated silica (Hi-Sil 190G)	Si190	2.2	
	carbon black (Vulcan 8)	CB110	1.9	

Fourier Transform Infrared Spectroscopy. Fourier transform infrared (FTIR) spectroscopy of powdered silica samples was performed on a Nicolet 6700 FTIR spectrometer. The FTIR spectra of the precipitated silica used in this study, Si190, were compared with those of the commercial fumed silica similar to the one used by Jin et al.[14] as shown in Figure 3. The −OH stretching mode in silanols is generally observed in the 3200−3800 cm^{-1} region. The inset of Figure 3 shows a marked difference in the surface −OH groups for Si190 as opposed to fumed silica. This observation indicates that the density of silanol functional groups on the surface of precipitated silica is greater than that of fumed silica in accordance with Croissant and Brinker.[31]

Small-Angle X-ray Scattering. Approximately 1 mm thick specimens for scattering studies were pressed from the milled nanocomposites under application of heat (∼100 °C) and pressure (2 bar) in a laboratory oven for 10 min. Ultra-SAXS (USAXS) and SAXS measurements were performed at beamline 9-ID-C operated by the X-ray Science Division at the Advanced Photon Source (APS) at Argonne National Laboratory. This instrument is designed by Jan Ilavsky and was operated using a synchrotron radiation of 0.5904 Å.[37,38] The USAXS/SAXS scans were recorded from three different positions on the sample for statistics. The scattered intensity from the

https://dx.doi.org/10.1021/acs.macromol.9b02429
Macromolecules 2020, 53, 2235−2248

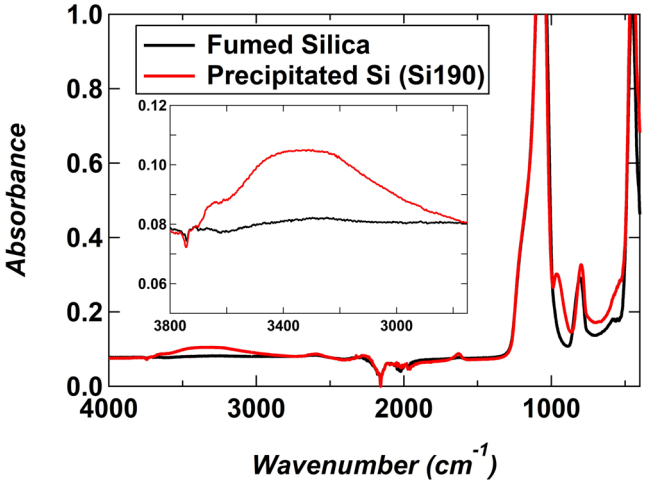

Figure 3. FTIR spectra (absorbance vs wavenumber) for precipitated silica (Si190) and commercial fumed silica; in the range of 2800−3800 cm^{-1}, a broad peak associated with silanol surface groups is observed for precipitated silica, which is absent for fumed silica (inset).

specimens was measured in the range of 0.0001 $Å^{-1} \leq q \leq 1$ $Å^{-1}$ traversing 4 decades in size. This was achieved through a combination of pinhole SAXS and Bonse−Hart USAXS instruments with a slit length of 0.8 × 0.8 mm. The USAXS data were desmeared to account for slit smearing. The relevant q-range for this study is 0.0001 $Å^{-1} \leq q \leq 0.1$ $Å^{-1}$ because the structural hierarchies over multiple length scales are accessible in this range. The SAXS and USAXS data sets were reduced, desmeared (I_{dsm} vs q curves for neat and filled polymers, 4526 and 4526HM, are shown in Figures S1 and S2 in the Supporting Information, respectively), corrected for background scattering from the polymer, and then merged using the absolute scale of the USAXS measurements. It is to be noted that the I_{dsm} for 4526 and 4526HM shows a broad knee at intermediate q (0.001 $Å^{-1} < q < 0.01$ $Å^{-1}$) associated with the blockiness of SBR as shown in Figures S1 and S2 in the Supporting Information. However, this knee intensity is much weaker than the signal from both dilute ($\phi \approx 0.005$) and semidilute ($\phi \approx 0.08$) curves. Additionally, multiple scattering effects were negligible as can be easily determined in the USAXS pattern. The Nika and Irena packages for Igor Pro were employed to reduce, desmear, and merge the data sets.[39,40] For all dilute samples ($\phi \approx 0.005$), the combined SAXS and USAXS curves were fit using the Unified Scattering Function shown in eqs 1 and 2. The squared difference in scattering length density was calculated from the scattering contrast calculator tool available in the Irena package for Igor Pro.

Transmission Electron Microscopy. Transmission electron micrographs of the milled nanocomposites were obtained from ∼80 nm sections sliced on a cryo-ultramicrotome below the glass-transition temperature of the matrix polymer. These thinly sliced sections were collected on 200-mesh carbon-coated copper support grids prior to TEM imaging operated in STEM mode. The microscope was operated with an accelerating voltage of 25 kV and an emission current of 10 μA.

RESULTS

Carbon Black Nanocomposites. Figure 4 shows the scattered intensity $I_0(q)/\phi_0$ versus q for a dilute sample ($\phi_0 \approx 0.005$) of 4526HM rubber filled with CB110. In reciprocal space, the lowest q region, $q < 0.0009$ $Å^{-1}$, contains information of the largest hierarchical structure observable in the combined USAXS/SAXS range. In this range, a power law slope of approximately −4 is attributed to compact agglomerated carbon black aggregates, which appear solid at

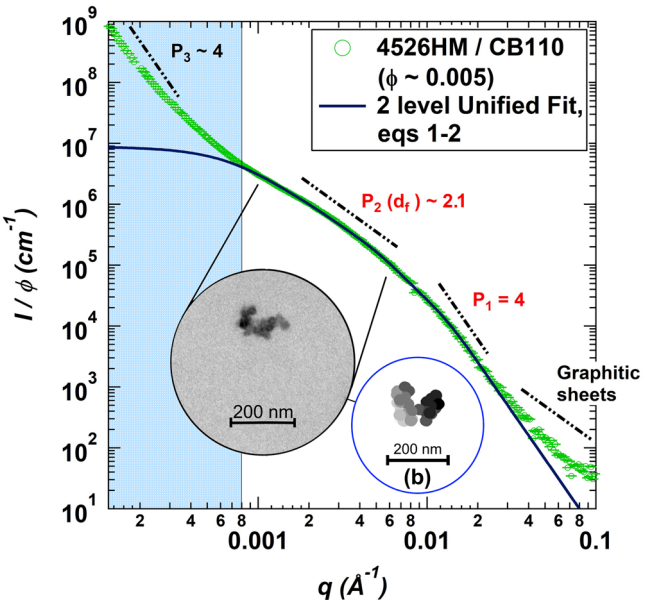

Figure 4. Log−log plot of the dilute-reduced scattered intensity $I_0(q)/\phi_0$ ($\phi_0 \approx 0.005$) vs the scattering vector q for carbon black, CB110, dispersed in 4526HM SBR. A two-level Unified fit was performed on the data (eq 1) indicated by the solid blue line with the fit parameters for the first two structural levels listed in Table 2. The region with a slope of −4 from 0.014 to 0.03 $Å^{-1}$ is associated with Porod scattering from the smooth surface of primary particles. The slope from 0.002 to 0.007 $Å^{-1}$ is associated with the scattering from mass fractal silica aggregates with $d_f = 2.1 \pm 0.1$. (a) TEM micrograph of a CB110 aggregate composed of a few sintered primary particles (in a similar butadiene rubber) and (b) simulated CB110 aggregate with the same structural parameters as the scattering result following Mulderig et al.,[41] indicating agreement between scattering and TEM.

micron length scales. Although the Guinier region, indicative of the feature size, is not observed, these agglomerates are larger than the observable q-range, which extends to a few microns. In the intermediate q range, $0.0009 < q < 0.024$ $Å^{-1}$, a power law slope of about −2.2 corresponds to carbon black fractal aggregates. It is followed by another slope of −4 indicative of scattering from smooth and sharp interfaces. This observation is attributed to the carbon black primary particles that are made of layered graphitic sheets, observed in the highest q region, $0.03 < q < 0.1$ $Å^{-1}$, with a power law of −2. The region between the fractal and surface scattering shows a weak Guinier knee related to the radius of gyration of the primary particles. Likewise, in the region between low and intermediate q, another Guinier knee can be observed, which corresponds to the radius of gyration of the mass fractal aggregates. In Figure 4, a two-level Unified fit from eqs 1 and 2, indicated by the solid blue line, is performed in the intermediate region, $0.0009 < q < 0.024$ $Å^{-1}$, and the fitted structural parameters for the first two levels are listed in Table 2. Table 2 also lists the fit parameters for 4526/CB110 nanocomposite (a plot of $I_0(q)/\phi_0$ vs q is not shown). For the same filler, the structural fits under dilute concentrations are expected to result in similar values within error, independent of the matrix type.

The fit parameters obtained from the Unified fit, listed in Table 2, can be used to calculate a variety of structural and topological parameters for different structural levels. The Sauter mean diameter (diameter of a sphere with the same specific surface area as that of the primary particle) is given by

https://dx.doi.org/10.1021/acs.macromol.9b02429
Macromolecules 2020, 53, 2235−2248

Table 2. Fit Parameters Obtained from the Unified Fit (eq 1) for Dilute-Reduced Scattering Curves, $I_0(q)/\phi_0$, Where $\phi_0 \approx 0.005$ for Precipitated (Si190) and Carbon Black (CB110) Nanocomposites

	level 1 Unified fit—primary particle				level 2 Unified fit—mass fractal aggregate			
nanocomposite	$G_1 \times 10^5$ (cm^{-1})	$R_{g,1}$ (nm)	$B_1 \times 10^{-4}$ (cm^{-1} Å^{-4})	P_1	$G_2 \times 10^6$ (cm^{-1})	$R_{g,2}$ (nm)	B_2 (cm^{-1} Å$^{-P_2}$)	P_2
4526HM/CB110	2.4 ± 0.1	31 ± 1	4.1 ± 0.1	4	9 ± 1	220 ± 30	2.6 ± 0.8	2.1 ± 0.05
4526/CB110	2.5 ± 0.1	32 ± 1	4.2 ± 0.1	4	8 ± 1	200 ± 20	2.3 ± 0.7	2.1 ± 0.04
4526HM/Si190	0.2 ± 0.1	9 ± 0.2	16 ± 2	4	62 ± 20	295 ± 20	0.4 ± 0.1	2.4 ± 0.1
4526/Si190	0.2 ± 0.1	9 ± 0.2	13 ± 1	4	70 ± 7	305 ± 10	0.2 ± 0.03	2.5 ± 0.1

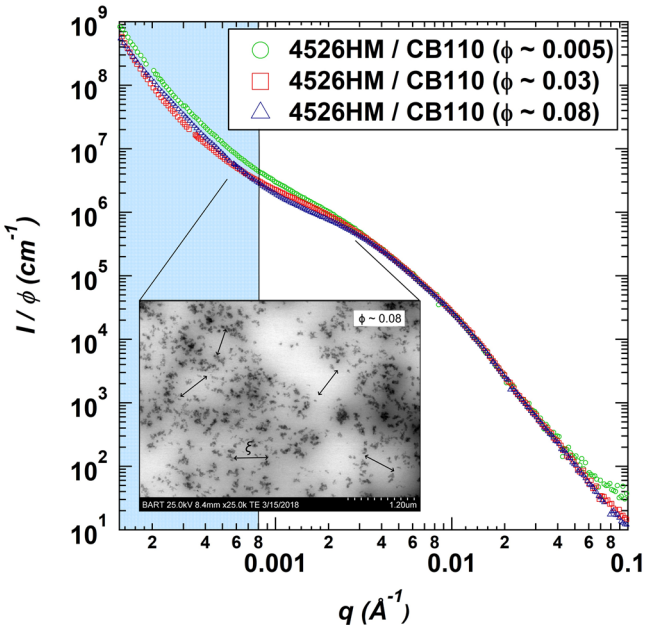

Figure 5. Log−log plots of the reduced scattered intensity $I(q)/\phi$ vs the scattering vector q for CB110 dispersed in 4526HM under dilute ($\phi \approx 0.005$) and semidilute ($\phi \approx 0.03$, 0.08) concentrations. The diminution in reduced scattered intensity can be modeled through the mean-field RPA to quantify the screening parameter, υ, through eq 4. The inset shows a TEM micrograph for $\phi \approx 0.08$ CB110 (in a similar butadiene rubber), indicating a close to random dispersion of aggregates and an average mesh size.

$d_p = 6\left(\frac{S}{V}\right)^{-1} = 6\left(\frac{B_1}{2\pi\langle\Delta\rho\rangle^2}\right)^{-1}$.[11] The degree of aggregation, $z = \left(\frac{G_2}{G_1}\right) + 1$, is the average number of primary particles within an aggregate determined from the ratio of the Guinier prefactors in the Unified fit (eqs 1 and 2).[42] The aggregate end-to-end distance, $R_{eted} = d_p z^{1/d_f}$, is related to the Sauter mean diameter, the degree of aggregation, and the mass fractal dimension, $d_f = P_2$. For the 4526HM/CB110 nanocomposite, d_p, z, and R_{eted} were estimated to be about 27 (±1) nm, 38 (±5), and 160 (±10) nm, respectively. d_p as calculated from the specific surface area ($d_{SSA} \approx 26$ nm) and the R_{eted} from the inset micrograph in Figure 4a (approximately three quarters of the scale bar ~150 nm) agree with the scattering measurements. Figure 4b shows a simulated CB110 aggregate following Mulderig et al.[41] The scattering results agree with the aggregate tortuosity parameters from the simulation as listed in Table S1 in the Supporting Information.

Figure 5 compares the reduced scattered intensity for the dilute ($\phi \approx 0.005$) and semidilute ($\phi \approx 0.03$, 0.08) samples of 4526HM/CB110. It is to be noted that these semidilute volume fractions represent local percolation, that is, overlap of nanoaggregates.[5] At much higher volume fractions, $\phi \approx 0.2$, the system percolates globally forming a micron-scale network.[5] Restricting the present discussion to concentrations below the global percolation threshold limits the interactions between nanoaggregates to predominant binary interactions allowing for a first-order approximation. In the high-q region, $0.006 < q < 0.04$ Å^{-1}, the two curves are well superimposed. However, in the intermediate and low-q regions, $q < 0.006$ Å^{-1}, the reduced scattered intensity of the semidilute curve diminishes and is attributed to overlapping nanoaggregates as represented in the inset of Figure 5 for $\phi \approx 0.08$. As discussed previously, this reduction due to binary interactions is related to the second virial coefficient that can be determined from eq 7. The decrement in scattered intensity quantified by the screening parameter, υ, is determined from the mean-field RPA as discussed below. Similar plots for 4526/CB110 nanocomposites are shown in Figure S3 in the Supporting Information.

The structure factor from eq 5 for $\phi \approx 0.03$ and 0.08 is plotted in Figure 6a,b, respectively, as a function of the reciprocal space vector, q. The data in Figure 6 is fit to eq 6, which describes the RPA, to obtain υ. For both semidilute volume fractions, in the limit of high-q, $S(q)$ equals 1, indicating that the increasing concentration has no effect on primary particle structure as is expected. A reduction in $S(q)$ at intermediate q is analogous to the diminution in reduced scattering intensity as can be seen in Figure 5. The mean-field approach, modeled by the RPA equation, agrees with the experimental data.

The low-q regions, indicated by the shaded blue areas in Figure 6a,b, deviate from the RPA fit because of the presence of large-scale structures. Nonetheless, the intercept at $q = 0$ is proportional to the extent of nanoaggregate screening, $1/(\phi\upsilon)$. The intercept for $\phi \approx 0.03$ is larger than for $\phi \approx 0.08$ confirming the same. The estimated υ from the fits and the computed pseudo-second virial coefficient, A_2, from eq 7 are listed in Table 3 for both the 4526HM/CB110 and 4526/CB110 nanocomposites. For both volume fractions, υ is approximately constant within the experimental error, indicating that the system is below the global percolation limit. For $\phi \approx 0.08$, the correlation length, $\xi_{RPA} = 2\pi/q_{RPA}$, where $q_{RPA} \approx 0.0009$ Å^{-1}, is the reciprocal scattering vector at which the RPA fit deviates from the experimental data. ξ_{RPA} is about 700 nm in agreement with the mesh size (about 600 nm or about half the scale bar) observed in the TEM micrograph in the inset to Figure 5.

Precipitated Silica Nanocomposites. Figure 7 shows the dilute-reduced scattered intensity, $I_0(q)/\phi_0$, versus q for 4526HM rubber filled with precipitated silica Si190. These data were subsequently fit to the three-level Unified Scattering Function in eqs 1 and 2. The fit parameters for the first two structural levels are listed in Table 2. A three-level fit was chosen because of the lack of a distinct Guinier knee region for

https://dx.doi.org/10.1021/acs.macromol.9b02429
Macromolecules 2020, 53, 2235−2248

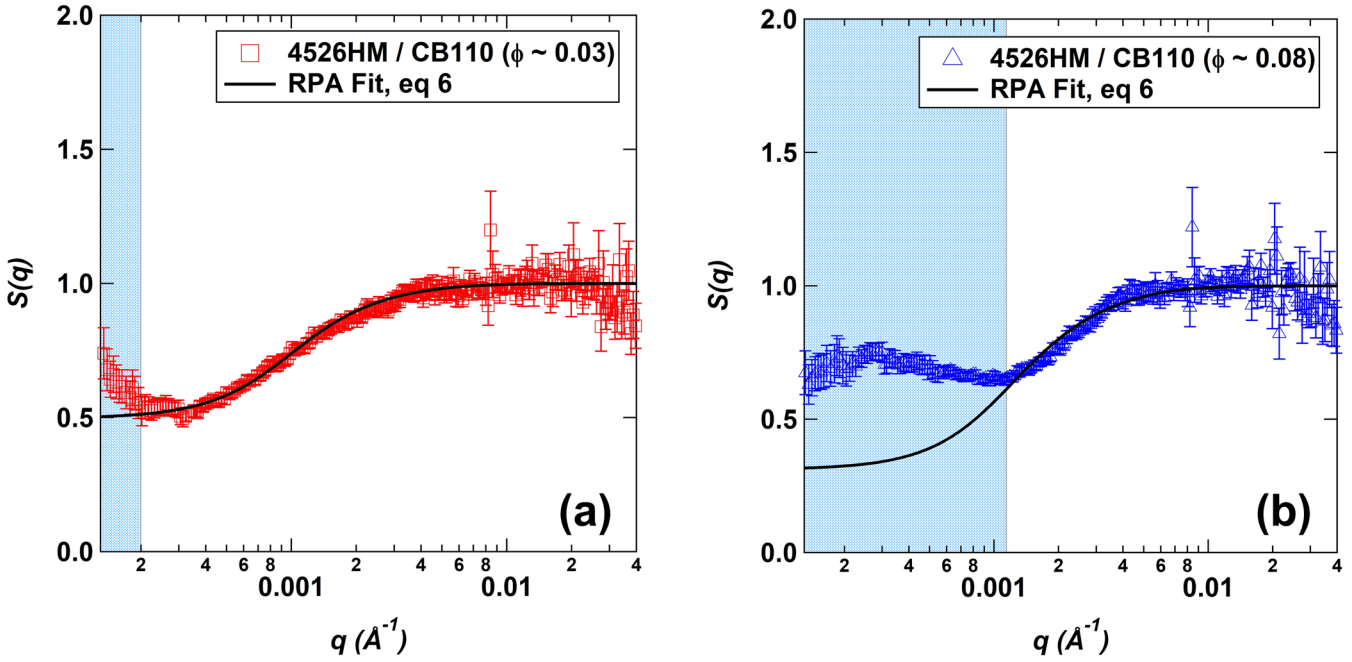

Figure 6. Mean field behavior as displayed in a plot of the structure factor, $S(q)$, vs the scattering vector, q, for CB110 dispersed in 4526HM with $\phi \approx 0.03$ (a) and $\phi \approx 0.08$ (b). The absence of a peak in either case indicates the lack of structural correlations. RPA fits, eq 6, were performed on both data sets to compute the screening parameter, υ, which is listed in Table 3. The shaded blue region is dominated by large-scale structures.

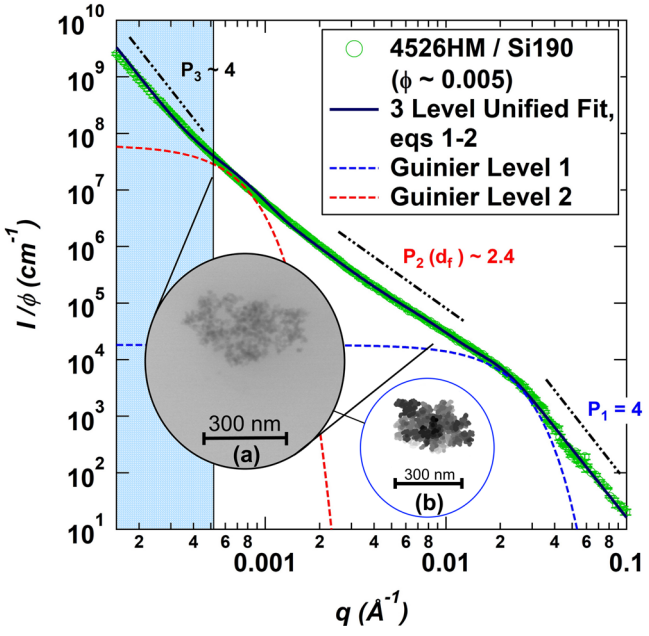

Figure 7. Log−log plot of the dilute-reduced scattered intensity $I_0(q)/\phi_0$ vs the scattering vector q for precipitated silica, Si190, dispersed in 4526HM SBR. A three-level Unified fit indicted by a solid black line was performed on the data using eq 1. The fit parameters for the first two structural levels are listed in Table 2. The region with a slope of −4 from 0.04 to 0.1 Å^{-1} is associated with Porod scattering from the smooth surface of primary particles. The slope from 0.007 to 0.02 Å^{-1} is associated with the scattering from mass fractal silica aggregates with $d_f = 2.4 \pm 0.1$. Additionally, a slope of −4 at lowest q indicates the presence of large silica agglomerates. (a) TEM micrograph of a Si190 aggregate composed of many sintered primary particles and (b) simulated Si190 aggregate with the same structural parameters as the scattering result following Mulderig et al.[41]

structural level 2 in $0.0005 < q < 0.002$ Å^{-1} in Figure 7, although this region is clearly distinguishable for 4526HM/CB110 in Figure 4. Similar to the carbon black CB110 discussed above, the lowest q, $q < 0.001$ Å^{-1}, is marked by a −4 power law slope characteristic of mesoscale agglomerates. At intermediate q, $0.001 < q < 0.01$ Å^{-1}, the power law slope of -2.4 ± 0.1 equals the negative of the mass fractal dimension, d_f, for the silica aggregates. Porod scattering with a power law slope of −4 in the high q region, $0.03 < q < 0.1$ Å^{-1}, reflects surface scattering from primary particles.

The key structural dissimilarity between precipitated silica and carbon black mixed with SBR 4526HM is the difference in the magnitude of the Guinier prefactors, G_1 and G_2, which reflects the average degree of aggregation, z. z for Si190 in 4526HM is estimated to be 3300 (±600), which is considerably larger than that observed for carbon black. This difference is evident in the inset micrographs of Si190 and CB110 nanoaggregates in Figures 4a and 7a. Additionally, d_p is estimated to be ∼12 nm. The aggregate end-to-end distance R_{eted} was estimated to be 360 (±30) nm in agreement with the inset micrograph in Figure 7a (slightly larger than the full scale bar ∼350 nm). Figure 7b shows a simulated Si190 aggregate from scattering following Mulderig et al.[41] The scattering results agree with the aggregate tortuosity parameters from simulation as listed in Table S1 in the Supporting Information.

Figure 8 compares the reduced scattered intensity for the dilute ($\phi \approx 0.005$) and semidilute ($\phi \approx 0.08$) samples of 4526HM/Si190. In the high-q region, $0.01 < q < 0.06$ Å^{-1}, the two curves superimpose well. However, in the intermediate region, $0.001 < q < 0.01$ Å^{-1}, the reduced scattered intensity presents a broad peak characteristic of strongly correlated structures. The inset micrograph in Figure 8 shows aggregated domains with different correlation lengths indicated by white dotted circles that are attributed to the combined effect of charged surface hydroxyl groups as well as the varying accumulated strain through the sample. The inset image in

https://dx.doi.org/10.1021/acs.macromol.9b02429
Macromolecules 2020, 53, 2235−2248

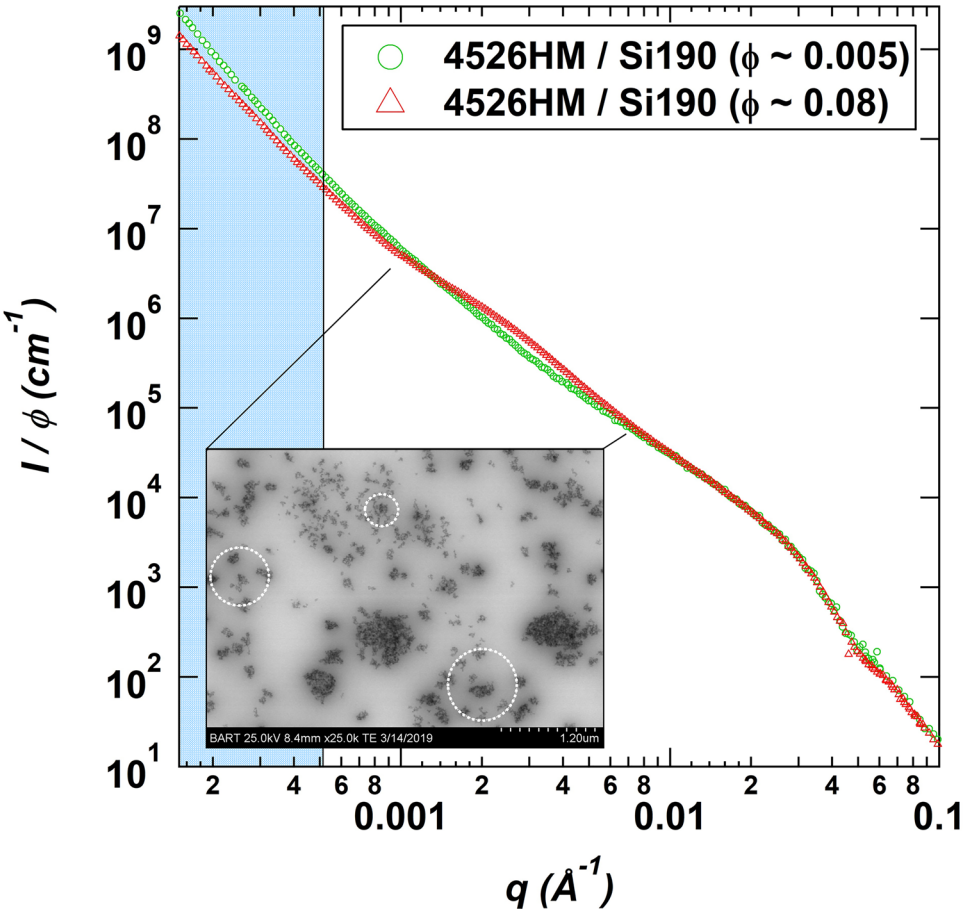

Figure 8. Log−log plots of the reduced scattered intensity $I(q)/\phi$ vs the scattering vector q for Si190 dispersed in 4526HM under dilute ($\phi \approx 0.005$) and semidilute ($\phi \approx 0.08$) concentrations. The presence of a correlation peak is indicative of specific interactions modeled via the polydisperse Born−Green approach to determine the mean correlation distance, $\langle\xi\rangle$, through eqs 13−15. $\langle\xi\rangle$ is related to the screening parameter from scattering via eq 16. A TEM micrograph for $\phi \approx 0.08$ Si190 shows the presence of aggregated domains with a distribution in correlation distances (inset).

Table 3. Fit Parameters for Carbon Black Nanocomposites from Mean Field RPA in eq 6, Where $I_0(q)/\phi_0$ Is Determined from the Unified Fit Parameters in eqs 1 and 2[a]

nanocomposite	ϕ	υ ($\times 10^{-6}$ cm)	ξ_{RPA} (nm)	A_2 ($\times 10^{-8}$ mol cm^3/g^2)
4526HM/CB110	0.03	3.2 ± 0.1	3900 ± 200	0.38 ± 0.01
4526HM/CB110	0.08	3.3 ± 0.1	700 ± 30	0.40 ± 0.01
4526/CB110	0.03	3.5 ± 0.1	3700 ± 150	0.42 ± 0.01
4526/CB110	0.08	3.6 ± 0.1	650 ± 20	0.43 ± 0.01

[a]Additionally, the pseudo-second virial coefficient, A_2 is computed from eq. 7

Table 4. Fit Parameters for Precipitated Silica, Si190, in 4526HM from the Polydisperse Born−Green, the Percus−Yevick, and the Born−Green Models in eqs 13−15 and 9, 10 and 11, 12, Respectively[a]

nanocomposite	fit type	ϕ	P	$\langle\xi\rangle$ or ξ (nm)	σ
4526HM/Si190	polydisperse Born−Green	0.08	8.9 ± 0.4	330 ± 10	0.66 ± 0.03
4526HM/Si190	Born−Green	0.08	1 ± 0.1	330 ± 3	
4526HM/Si190	Percus−Yevick	0.08		350 ± 6	

[a]The fits are shown in Figure 9.

Figure 8 supports the hypothesis in Figure 2b. The correlated domains of precipitated silica nanoaggregates are distinctly different from the randomly dispersed carbon black nanoaggregates. However, in the low-q region, $q < 0.001$, the intensity diminishes. In the context of the present discussion, this observation means that strong interactions that lead to correlated structures is a phenomenon restricted to the nanoaggregates with charged surface hydroxyl groups, whereas, at larger size scales, the correlations are not observable and the silica system is analogous to the carbon black mean-field system. Similar plots for 4526/Si190 nanocomposites are shown in Figure S4 in the Supporting Information.

The correlation peak shown in Figure 8 is interpreted through the structure factor for $\phi \approx 0.08$ silica in 4526HM

https://dx.doi.org/10.1021/acs.macromol.9b02429
Macromolecules 2020, 53, 2235−2248

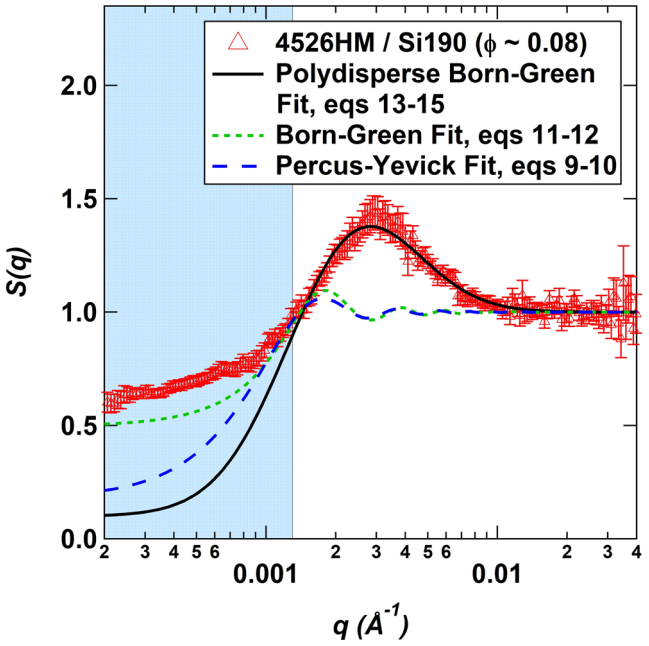

Figure 9. Plot of the structure factor, $S(q)$, vs the scattering vector, q, for Si190 dispersed in 4526HM rubber containing a $\phi \approx 0.08$ nanofiller. A peak in the structure factor occurs at $q \approx 0.003$ that was fit using the polydisperse Born−Green approach proposed in eqs 13−15 indicated by the solid black line to calculate the average correlation distance, $\langle\xi\rangle$, and subsequently the screening parameter, υ. The fit is compared with the Percus−Yevick (eqs 9 and 10) and Born−Green (eqs 11 and 12) approximations indicated by the dashed blue and the dotted green lines, respectively. The shaded blue region is dominated by large-scale structures.

shown in Figure 9. Because various aggregated domains in the system display different preferred distances for structural correlation, the proposed polydisperse Born−Green approach (indicated by a solid black line) in eqs 13−15 is fit to the structure factor in Figure 9. This fit is contrasted with the traditional Percus−Yevick (indicated by a dashed blue line) and Born−Green (indicated by a dotted green line) approximations from eqs 9, 10 and 11, 12 respectively. The structure factor fit to the polydisperse Born−Green function, eqs 13−15, approximates the data well in the range where low-q agglomerates do not impact the structure factor. The blue area in Figure 9 corresponds to the region dominated by the low-q agglomerate structure.

The fit parameters listed in Table 4 indicate a packing factor, p, of about 8.9 (±0.4). Although for hard spheres, $0 \leq p \leq 5.92$,[25] the silica aggregates are asymmetric mass fractal structures that could have a greater packing factor due to enhanced interpenetration and alignment of the asymmetric aggregates. The value of $\langle\xi\rangle$ was found to be 330 (±10) nm in agreement with previous mesh size measurements on a similar system comprising Si190 dispersed in polyisoprene.[14] Although the Percus−Yevick and Born−Green fits return similar values of the mesh size, $\langle\xi\rangle$, the fits are poor and neither include the existence of domains with different correlation lengths nor account for arrangement/packing of mass fractal structures as observed in scattering and microscopy in Figure 8. Note that $2\pi/q_{peak}$ in Figure 9 does not correspond with ξ due to the large polydispersity in domain spacing, $\sigma = 0.66$.

For the precipitated silica filler, the analysis based on the solutions to the Ornstein−Zernike equation, presented above, deviate because of the large polydispersity in all features of the system. For systems with charged surfaces, the approach presented here may be useful. The polydisperse Born−Green model was also tested on precipitated silica and colloidal silica systems from the literature. Jin et al. measured the USAXS scattering from Si190 mixed with two grades of polybutadiene, viz., B45 (Mooney viscosity of 45 M.U., 38% cis content) and 140ND (Mooney viscosity of 42 M.U., 96% cis content).[14] For both systems, the mean-field approach did not work because of the presence of correlation peaks in scattering. These two systems have been analyzed through the polydisperse Born−Green model presented here and the fits are shown in Figure 10a,b. The proposed model fits the curves well above $q \approx 0.002$ Å^{-1}, below which (indicated by the shaded blue region) the deviation is attributed to large silica agglomerates as observed at lowest q in the $I_0(q)/\phi_0$ plot in Figure 7. The screening parameter (from the mean-field approach) can be determined from the mesh size averaged over all correlated domains available directly from the fits using eq 16. The

Table 5. Fit Parameters from the Polydisperse Born−Green Approach (eqs 13−15) for Precipitated Silica Nanocomposites and the Polydisperse Born−Green Fit with Modifications (eq 17) for Colloidal Silica Nanospheres[a]

nanocomposite	fit type	p	$\langle\xi\rangle$ (nm)	σ	δ	υ (×10^{-6} cm)	A_2 (×10^{-8} mol cm^3/g^2)
4526HM/Si190	polydisperse Born−Green	8.9 ± 0.4	330 ± 10	0.66 ± 0.03		11 ± 1	2.0 ± 0.2[b]
4526/Si190	polydisperse Born−Green	9.1 ± 0.2	300 ± 30	0.62 ± 0.08		12 ± 1	2.2 ± 0.2[b]
B45/Si190[14]	polydisperse Born−Green	8.8 ± 0.1	177 ± 1	0.37 ± 0.01		44 ± 2	11 ± 0.6
140ND/Si190[14]	polydisperse Born−Green	10.6 ± 0.1	176 ± 1	0.48 ± 0.01		33 ± 1	8 ± 0.3
PEODME (1000 g/mol)/Col. Si[27]	polydisperse Born−Green with modification	4.4 ± 0.1	61 ± 1	0.2 ± 0.1	0.4 ± 0.1		
PEODME (2000 g/mol)/Col. Si[27]	polydisperse Born−Green with modification	4.3 ± 0.2	61 ± 1	0.2 ± 0.1	0.4 ± 0.1		

[a]The correlation distance averaged over all domains, $\langle\xi\rangle$, is used to determine the screening parameter, υ, from eq 16, which was then used to obtain A_2 from eq 7. [b]Other than the difference in the scattering length density which affects the scattering contrast and thereby A_2, the processing conditions of the samples were different. Jin et al.[14] milled their silica nanocomposites for 6 min, whereas in this study, the mixing time was 20 min. Rishi et al.[16] have detailed the effects of mixing time such that longer mixing times result in larger values of A_2, related to better nanodispersion. Additionally, A_2 is sensitive to the fit parameters from the dilute scattering curve. In scattering, the Guinier knee corresponding to level 2 (aggregate level) for silica is sometimes obscured by agglomerates of aggregates (level 3), which could possibly result in erroneous values. Jin et al.[14] attempted a two-level fit on their Si190-PI(polyisoprene) sample. This was corrected in this study by fitting all silica samples to a three-level Unified fit including the agglomerate structure.

https://dx.doi.org/10.1021/acs.macromol.9b02429
Macromolecules 2020, 53, 2235−2248

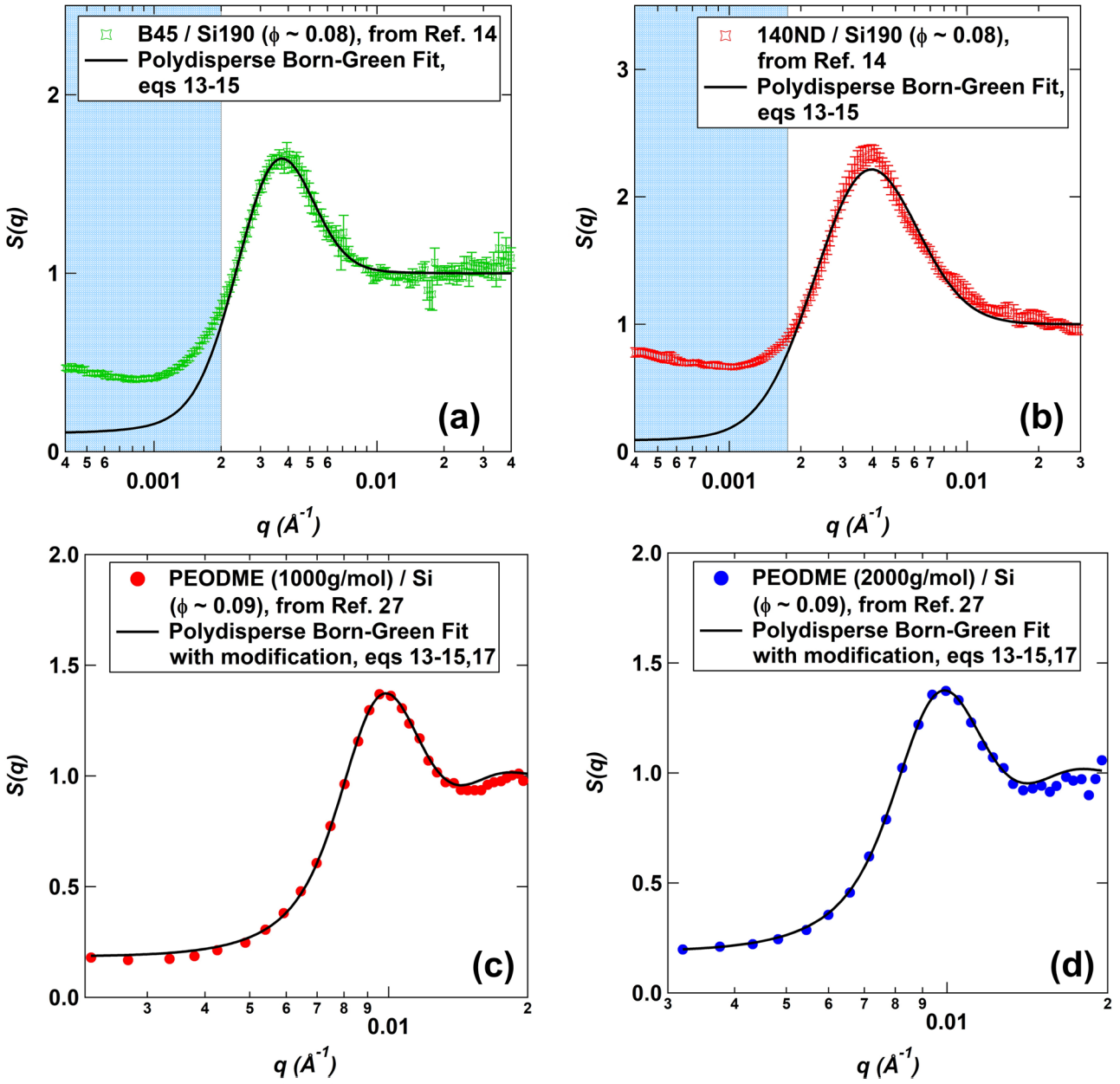

Figure 10. Structure factor, $S(q)$, as a function of reciprocal space vector, q, for precipitated silica in two polybutadiene matrices, viz., (a) B45 and (b) 140ND from Jin et al.[14] Structure factor, $S(q)$, as a function of reciprocal space vector, q, for colloidal silica nanospheres dispersed in PEODME with two different molecular weighs, viz., (c) 1000 and (d) 2000 g/mol from Anderson and Zukoski.[27] The data in (a) and (b) are fit using the polydisperse Born−Green approach in eqs 13−15, whereas the data in (c,d) were fit using a modification to the proposed polydisperse Born−Green approach in eq 17. The silica nanospheres in (c,d) do not display agglomerates so that the data can be fit to the $q \rightarrow 0$ limit.

pseudo-second virial coefficient, A_2, is then determined from eq 7. These values are listed in Table 5.

Additionally, Anderson and Zukoski[27] measured the structure factors for colloidal silica nanospheres in polyethylene oxide dimethyl ether (PEODME) with different molecular weights as shown in Figure 10c,d. The structure factors in Figure 10c,d indicated the presence of a strong correlated peak with a maximum at $q \approx 0.01$ Å^{-1}. A broad second-order peak is observed at about 0.02 Å^{-1}. In order to better fit the entire q-range of structure factor, the value of q in eq 15 is modified as follows,

$$q_{\mathrm{mod}} = q \exp\left\{\delta \frac{(q - q_{\mathrm{peak}})}{q}\right\} \tag{17}$$

where $q_{\mathrm{peak}} = 2\pi/\xi$ corresponds to the q-value of the peak in the structure factor. δ is a parameter related to disorder. This empirical correction allows the fit to better match the low-intensity portion at low q and the second-order peak at high q. A plot of q_{mod} (eq 17) as a function of reciprocal space vector, q_{mod} with $q_{\mathrm{peak}} \approx 0.01$ Å^{-1}, is shown in Figure S5 in the Supporting Information. Tabulated fit values for the PEODME colloidal silica systems are listed in Table 5.

Figure 11a compares the packing factor, p, for precipitated silica (Si190) and colloidal silica in different matrices. For

https://dx.doi.org/10.1021/acs.macromol.9b02429
Macromolecules 2020, 53, 2235−2248

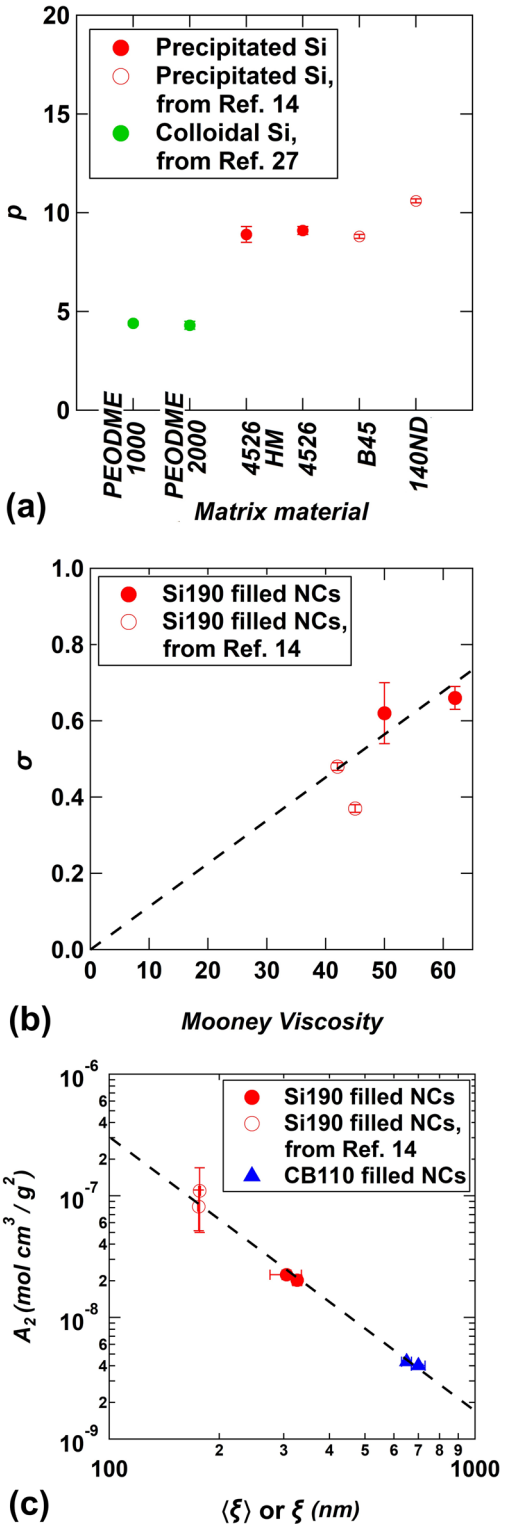

Figure 11. (a) Packing factor, p, from the polydisperse Born−Green fits to the structure factors for precipitated (Si190) and colloidal silica[27] nanocomposites with a larger p attributed to the fractal nature of silica aggregates and the silanol density on the surface. (b) Geometric standard deviation, σ, for precipitated silica nanocomposites used this study and from ref 14 as a function of the Mooney viscosity of the polymer matrix. (c) Dependence of the interaction potential, A_2, on the mesh size/correlation length for CB110, Si190, and colloidal silica nanocomposites.

Si190, irrespective of the matrix polymer, the packing factor is much larger than for colloidal silica and is greater than the maximum value of 5.92 for closest packed spheres. This is the result of the asymmetric and open fractal structure of Si190 aggregates compared to almost perfect spheres for colloidal silica as well as possibly stronger filler−filler interactions. The density of silanol functional groups on the surface of precipitated silica is greater than for colloidal silica.[31]

Figure 11b shows the geometric standard deviation, σ, which reflects the distribution of correlation distances as shown in Figure 2b. Values are given for the precipitated silica samples as a function of the Mooney viscosities of the polymer matrices. Because σ indicates the breadth of the distribution of correlation distances, it is expected that for less viscous matrices, the accumulated strain will be more uniform, leading to a narrower distribution of correlation lengths. For in situ generated silica,[25] there is no accumulated strain because the samples are fabricated from low-viscosity prepolymers and a close to monodisperse distribution of correlation lengths is observed (Figure 2a). Figure 11b shows that σ increases with increasing matrix viscosity, which is expected as the total accumulated strain experienced during milling is a sensitive function of the matrix viscosity.

Figure 11c shows a log−log plot of the computed pseudo-second-order virial coefficient, A_2, as a function of the average correlation distance $\langle\xi\rangle$ or ξ for precipitated silica (Si190) and carbon black (CB110) nanocomposites, respectively. A power-law dependence of the interaction potential with the structural correlation distance, $A_2 \approx (\xi)^{-2}$, for all of the studied systems indicates the universal behavior for mass fractal aggregates such as silica and carbon black in these kinetically dispersed, immiscible systems. The power law approximates a function proposed by Mulderig et al.,[13] $\xi^{-d_f} \approx B_2\phi A_2$. Here, $d_f \approx 2.3$.

CONCLUSIONS

Dispersion in nanocomposites is governed by thermal diffusion, kinetic mixing, particle interactions, and particle/matrix compatibility. The combined impact can manifest into systems with variable degree of particle−particle correlation. Weakly interacting nanocomposites can be modeled using a mean-field approach, which leads to a description of dispersion based on the second virial coefficient and the filler network mesh size. Moderately correlated systems with specific interactions require a structure factor analysis, but the results can be translated into mesh size and second virial coefficient for comparison with mean-field nanocomposites. The nanoscale mesh size can be verified with microscopy in the semidilute regime. The presence of grains or domains of correlation with different correlation distances between mass fractal aggregates is evident in TEM micrographs. It was demonstrated that the carbon black filler in polybutadiene can be well described using a mean-field approach, while precipitated silica with surface hydroxyl groups displays specific interactions and must be modeled with moderate correlations. The resulting mesh size for the two systems is used to determine the pseudo-second-order virial coefficient, A_2. A_2, obtained in this way, is a measure of the relative quality of dispersion on the nanoscale for the two types of composites.

ASSOCIATED CONTENT

Supporting Information

The Supporting Information is available free of charge at https://pubs.acs.org/doi/10.1021/acs.macromol.9b02429.

https://dx.doi.org/10.1021/acs.macromol.9b02429
Macromolecules 2020, 53, 2235−2248

Comparison of the scattering and simulation results; reduced scattered intensity $I(q)/\phi$ and $S(q)$ versus q for 4526/CB110 at $\phi \approx 0.005$, 0.03, and 0.08; reduced scattered intensity $I(q)/\phi$ and $S(q)$ versus q for 4526/Si190 at $\phi \approx 0.005$, 0.08; and modified reciprocal space vector as a function of q based on eq 17 (PDF)

AUTHOR INFORMATION

Corresponding Author

Gregory Beaucage − *Chemical and Materials Engineering, University of Cincinnati, Cincinnati, Ohio 45221, United States;* orcid.org/0000-0002-6632-0889; Email: gbeaucage@gmail.com

Authors

Alex McGlasson − *Chemical and Materials Engineering, University of Cincinnati, Cincinnati, Ohio 45221, United States*

Kabir Rishi − *Chemical and Materials Engineering, University of Cincinnati, Cincinnati, Ohio 45221, United States;* orcid.org/0000-0002-3159-031X

Michael Chauby − *Chemical and Materials Engineering, University of Cincinnati, Cincinnati, Ohio 45221, United States*

Vikram Kuppa − *Nonstructural Materials Division, University of Dayton Research Institute, Dayton, Ohio 45469, United States*

Jan Ilavsky − *Advanced Photon Source, Argonne National Laboratory, Argonne, Illinois 60439, United States*

Mindaugas Rackaitis − *Bridgestone Americas Center for Research and Technology, Akron, Ohio 44301, United States*

Complete contact information is available at: https://pubs.acs.org/10.1021/acs.macromol.9b02429

Author Contributions

⊥Equal contribution by A.M. & K.R.

Notes

The authors declare no competing financial interest.

ACKNOWLEDGMENTS

This work was supported by the National Science Foundation through grants CMMI-1635865 and CMMI-1636036. A.M. and M.C. were supported by a Research Experience for Undergraduates supplemental grant CMMI-1761420 associated with CMMI-1635865. Use of the APS, an Office of Science User Facility operated for the U.S. Department of Energy (DOE) Office of Science by Argonne National Laboratory, was supported by the U.S. DOE under contract no. DE-AC02-06CH11357. The USAXS data were collected at the APS on the beamline 9-ID-C operated by the X-ray Science Division. The authors gratefully acknowledge the vital assistance of J.I. and his staff at 9-ID-C. The authors would also like to thank Julian Oberdisse and Anne-Caroline Genix for their feedback and input during the revision process as well as a more in-depth description of the work presented by Baeza et al.[8]

REFERENCES

(1) Kumar, S. K.; Benicewicz, B. C.; Vaia, R. A.; Winey, K. I. 50th Anniversary Perspective: Are Polymer Nanocomposites Practical for Applications? *Macromolecules* **2017**, *50*, 714−731.

(2) Potts, J. R.; Dreyer, D. R.; Bielawski, C. W.; Ruoff, R. S. Graphene-Based Polymer Nanocomposites. *Polymer* **2011**, *52*, 5−25.

(3) Kuilla, T.; Bhadra, S.; Yao, D.; Kim, N. H.; Bose, S.; Lee, J. H. Recent Advances in Graphene Based Polymer Composites. *Prog. Polym. Sci.* **2010**, *35*, 1350−1375.

(4) Das, A.; Kasaliwal, G. R.; Jurk, R.; Boldt, R.; Fischer, D.; Stöckelhuber, K. W.; Heinrich, G. Rubber Composites Based on Graphene Nanoplatelets, Expanded Graphite, Carbon Nanotubes and Their Combination: A Comparative Study. *Compos. Sci. Technol.* **2012**, *72*, 1961−1967.

(5) Rishi, K.; Beaucage, G.; Kuppa, V.; Mulderig, A.; Narayanan, V.; McGlasson, A.; Rackaitis, M.; Ilavsky, J. Impact of an Emergent Hierarchical Filler Network on Nanocomposite Dynamics. *Macromolecules* **2018**, *51*, 7893−7904.

(6) Filippone, G.; Romeo, G.; Acierno, D. Viscoelasticity and Structure of Polystyrene/Fumed Silica Nanocomposites: Filler Network and Hydrodynamic Contributions. *Langmuir* **2010**, *26*, 2714−2720.

(7) Filippone, G.; Salzano de Luna, M. A Unifying Approach for the Linear Viscoelasticity of Polymer Nanocomposites. *Macromolecules* **2012**, *45*, 8853−8860.

(8) Baeza, G. P.; Genix, A.-C.; Degrandcourt, C.; Petitjean, L.; Gummel, J.; Couty, M.; Oberdisse, J. Multiscale Filler Structure in Simplified Industrial Nanocomposite Silica/SBR Systems Studied by SAXS and TEM. *Macromolecules* **2013**, *46*, 317−329.

(9) Bouty, A.; Petitjean, L.; Degrandcourt, C.; Gummel, J.; Kwaśniewski, P.; Meneau, F.; Boué, F.; Couty, M.; Jestin, J. Nanofiller Structure and Reinforcement in Model Silica/Rubber Composites: A Quantitative Correlation Driven by Interfacial Agents. *Macromolecules* **2014**, *47*, 5365−5378.

(10) Beaucage, G. Approximations Leading to a Unified Exponential/Power-Law Approach to Small-Angle Scattering. *J. Appl. Crystallogr.* **1995**, *28*, 717−728.

(11) Beaucage, G.; Kammler, H. K.; Pratsinis, S. E. Particle Size Distributions from Small-Angle Scattering Using Global Scattering Functions. *J. Appl. Crystallogr.* **2004**, *37*, 523−535.

(12) Beaucage, G. Determination of Branch Fraction and Minimum Dimension of Mass-Fractal Aggregates. *Phys. Rev. E: Stat. Phys., Plasmas, Fluids, Relat. Interdiscip. Top.* **2004**, *70*, 10.

(13) Mulderig, A.; Beaucage, G.; Vogtt, K.; Jiang, H.; Jin, Y.; Clapp, L.; Henderson, D. C. Structural Emergence in Particle Dispersions. *Langmuir* **2017**, *33*, 14029−14037.

(14) Jin, Y.; Beaucage, G.; Vogtt, K.; Jiang, H.; Kuppa, V.; Kim, J.; Ilavsky, J.; Rackaitis, M.; Mulderig, A.; Rishi, K.; et al. A Pseudo-Thermodynamic Description of Dispersion for Nanocomposites. *Polymer* **2017**, *129*, 32−43.

(15) Vogtt, K.; Beaucage, G.; Weaver, M.; Jiang, H. Thermodynamic Stability of Worm-like Micelle Solutions. *Soft Matter* **2017**, *13*, 6068−6078.

(16) Rishi, K.; Narayanan, V.; Beaucage, G.; McGlasson, A.; Kuppa, V.; Ilavsky, J.; Rackaitis, M. A Thermal Model to Describe Kinetic Dispersion in Rubber Nanocomposites: The Effect of Mixing Time on Dispersion. *Polymer* **2019**, *175*, 272−282.

(17) Egelstaff, P. A. *An Introduction to the Liquid State*; Academic Press: London, New York, US, 1967.

(18) de Gennes, P. G. Theory of X-Ray Scattering by Liquid Macromolecules with Heavy Atom Labels. *J. Phys.* **1970**, *31*, 235−238.

(19) Percus, J. K.; Yevick, G. J. Analysis of Classical Statistical Mechanics by Means of Collective Coordinates. *Phys. Rev.* **1958**, *110*, 1−13.

(20) Guinier, A.; Fournet, G. *Small Angle Scattering of X-rays*; John Wiley & Sons: New York, US, 1955.

(21) Wang, M.-J.; Wolff, S.; Donnet, J.-B. Filler-Elastomer Interactions. Part I: Silica Surface Energies and Interactions with Model Compounds. *Rubber Chem. Technol.* **1991**, *64*, 559−576.

(22) Wang, M.-J.; Wolff, S.; Donnet, J.-B. Filler—Elastomer Interactions. Part III. Carbon-Black-Surface Energies and Interactions with Elastomer Analogs. *Rubber Chem. Technol.* **1991**, *64*, 714−736.

(23) Wolff, S.; Wang, M.-J. Filler—Elastomer Interactions. Part IV. The Effect of the Surface Energies of Fillers on Elastomer Reinforcement. *Rubber Chem. Technol.* **1992**, *65*, 329−342.

(24) Bouty, A.; Petitjean, L.; Chatard, J.; Matmour, R.; Degrandcourt, C.; Schweins, R.; Meneau, F.; Kwaśniewski, P.;

Boué, F.; Couty, M.; et al. Interplay between Polymer Chain Conformation and Nanoparticle Assembly in Model Industrial Silica/Rubber Nanocomposites. *Faraday Discuss.* **2016**, *186*, 325−343.
(25) Beaucage, G.; Ulibarri, T. A.; Black, E. P.; Schaefer, D. W. *Multiple Size Scale Structures in Silica—Siloxane Composites Studied by Small-Angle Scattering*; American Chemical Society, 1995; pp 97−111.
(26) Anderson, B. J.; Zukoski, C. F. Nanoparticle Stability in Polymer Melts As Determined by Particle Second Virial Measurement. *Macromolecules* **2007**, *40*, 5133−5140.
(27) Anderson, B. J.; Zukoski, C. F. Rheology and Microstructure of Polymer Nanocomposite Melts: Variation of Polymer Segment−Surface Interaction. *Langmuir* **2010**, *26*, 8709−8720.
(28) Jethmalani, J. M.; Ford, W. T.; Beaucage, G. Crystal Structures of Monodisperse Colloidal Silica in Poly(Methyl Acrylate) Films. *Langmuir* **1997**, *13*, 3338−3344.
(29) Bichoutskaia, E.; Boatwright, A. L.; Khachatourian, A.; Stace, A. J. Electrostatic Analysis of the Interactions between Charged Particles of Dielectric Materials. *J. Chem. Phys.* **2010**, *133*, 024105.
(30) Stace, A. J.; Bichoutskaia, E. Absolute Electrostatic Force between Two Charged Particles in a Low Dielectric Solvent. *Soft Matter* **2012**, *8*, 6210−6213.
(31) Croissant, J. G.; Brinker, C. J. *Biodegradable Silica-Based Nanoparticles: Dissolution Kinetics and Selective Bond Cleavage*; Elsevier: Amsterdam, The Netherlands, 2018; pp 181−214.
(32) McGlasson, A.; Rishi, K.; Beaucage, G.; Narayanan, V.; Chauby, M.; Mulderig, A.; Kuppa, V. K.; Ilavsky, J.; Rackaitis, M. The Effects of Staged Mixing on the Dispersion of Reinforcing Fillers in Elastomer Compounds. *Polymer* **2019**, *181*, 121765.
(33) Wertheim, M. S. Exact Solution of the Percus-Yevick Integral Equation for Hard Spheres. *Phys. Rev. Lett.* **1963**, *10*, 321−323.
(34) Roe, R.-J. *Methods of X-Ray and Neutron Scattering in Polymer Science*; Oxford university press: New York, US, 2000.
(35) McEwan, M. E.; Egorov, S. A.; Ilavsky, J.; Green, D. L.; Yang, Y. Mechanical Reinforcement of Polymer Nanocomposites: Theory and Ultra-Small Angle X-Ray Scattering (USAXS) Studies. *Soft Matter* **2011**, *7*, 2725.
(36) *Lognormal Distributions: Theory and Applications*; Crow, E. L., Shimizu, K., Eds.; CRC Press: Boca Raton, Florida, US, 1987.
(37) Ilavsky, J.; Zhang, F.; Andrews, R. N.; Kuzmenko, I.; Jemian, P. R.; Levine, L. E.; Allen, A. J. Development of Combined Microstructure and Structure Characterization Facility for in Situ and Operando Studies at the Advanced Photon Source. *J. Appl. Crystallogr.* **2018**, *51*, 867−882.
(38) Ilavsky, J.; Zhang, F.; Allen, A. J.; Levine, L. E.; Jemian, P. R.; Long, G. G. Ultra-Small-Angle X-Ray Scattering Instrument at the Advanced Photon Source: History, Recent Development, and Current Status. *Metall. Mater. Trans. A* **2013**, *44*, 68−76.
(39) Ilavsky, J.; Jemian, P. R. Irena: Tool Suite for Modeling and Analysis of Small-Angle Scattering. *J. Appl. Crystallogr.* **2009**, *42*, 347−353.
(40) Ilavsky, J. Nika: Software for Two-Dimensional Data Reduction. *J. Appl. Crystallogr.* **2012**, *45*, 324−328.
(41) Mulderig, A.; Beaucage, G.; Vogtt, K.; Jiang, H.; Kuppa, V. Quantification of Branching in Fumed Silica. *J. Aerosol Sci.* **2017**, *109*, 28−37.
(42) Vogtt, K.; Beaucage, G.; Weaver, M.; Jiang, H. Scattering Function for Branched Wormlike Chains. *Langmuir* **2015**, *31*, 8228−8234.

https://dx.doi.org/10.1021/acs.macromol.9b02429
Macromolecules 2020, 53, 2235−2248